Enhancing Electrochemical Performance, Bandgap Tunability, and Morphology Transition of CdS via Acoustic Shock Wave Exposure

F. Irine Maria Bincy[1], S. Oviya[1], Ikhyun Kim[2,*] and S. A. Martin Britto Dhas[1,2,*]

[1] *Shock Wave Research Laboratory, Department of Physics, Abdul Kalam Research Center, Sacred Heart College, Tirupattur, affiliated to Thiruvalluvar University, Tamil Nadu, 635 601, India*

[2] *Department of Mechanical Engineering, Keimyung University, Daegu 42601, Republic of Korea*

Abstract: As global demand for efficient energy storage systems increases, supercapacitors emerged as a promising candidate due to their high-power density, long cycle life, and rapid charge-discharge capability. Cadmium sulfide (CdS) is an II-VI semiconductor, offers potential as an electrode material but is limited by conventional synthesis routes that fail to optimize its structural and electrochemical characteristics. This current study introduces a novel method of acoustic shock wave treatment to enhance the electrochemical performance of CdS. Using a semi-automatic Reddy tube CdS is subjected to 300 shock pulses with a Mach number of 1.5, a pressure of 0.59 MPa, and a temperature of 520K, resulting in a XRD peak shift without structural degradation, bandgap reduction from 2.37 to 2.25 eV, and a morphology change from rod- to cube-shaped structures (FE-SEM). BET analysis revealed that the surface area increased from 1.07 to 2.10 m²/g and an average pore diameter reduction from 19.70 to 9.50 nm. Electrochemical measurements showed increased specific capacitance for 300 shock pulses from 266 to 268 F g^{-1} at 5 mV s^{-1} and from 128 to 142 F g^{-1} at 100 mV s$^{-1,}$ along with increased capacitive contribution from 75% to 78% at 5 mV s-1 and from 93% to 94% at 100 mV s-1 and improved ion diffusion kinetics. After 300 shock pulses sample also exhibited a significant reduction in bulk resistance from 6.613 × 10^{3} to 1.262 × 10^{3} Ω, increased bulk conductivity from 1.51 × 10^{-4} to 7.92 × 10^{-4} W m^{-1} K^{-1}, and enhanced bulk capacitance from 7.90 × 10^{-6} to 9.81 × 10^{-6} F. Additionally, cyclic stability improved, with capacitance retention rising from 63.3% to 71.4% after shock wave treatment. These results demonstrate the effectiveness of acoustic shock wave treatment in tailoring material properties for energy storage applications, offering a scalable strategy for the development of next-generation supercapacitor electrodes.

Keywords: CdS, Tunable bandgap, Morphology transition, Improved electrochemical performance.

INTRODUCTION

The increasing world population and increased technology demands have driven the need for energy security. For addressing the increasing demand for power in daily applications like portable electronics and hybrid vehicles, the development of low-cost and high-performance energy storage systems is imperative. Supercapacitors are emerging as alternative options to conventional batteries. They offer long cycle life, high power density, and rapid charging capability. These advantages make them sufficient for the energy needs of today. As global energy consumption continues to rise, supercapacitors provide a reliable and effective means of storage [1-4]. Several materials, such as carbon-based compounds, conducting polymers, and transition metal oxides, have been investigated for supercapacitor electrode applications. All the above-mentioned materials have huge advantageous qualities that can improve the performance of supercapacitors, such as high conductivity, stability, and energy storage. Scientists are continuing to investigate and develop these materials to improve the efficiency and sustainability of energy storage systems [5-8]. Among them, metal sulfide electrode materials have gained a lot of interest due to their high capacitance and fast redox kinetics. Especially, II-VI semiconductors show size-dependent nonlinear optical, electronic, and physical properties, which make them good candidates for extensive applications. Also, biological labeling, light-emitting diodes (LEDs), and nanoelectronics are included. Of these semiconductors, cadmium sulfide (CdS) is noteworthy with a direct band gap of 2.42 eV to support light emission at the blue to red wavelength range. CdS is also extensively applied in commercial devices like solar cells, photoelectronic devices, and heterogeneous photocatalysis [9-13].

Despite ongoing research into improving materials energy storage capacities through conventional approaches such as composites [14] and doping [15], they often fall short in simultaneously achieving key performance metrics such as high capacitance, efficient charge-discharge characteristics, and long-term structural stability. These limitations are largely attributed to their inherently complex and time-consuming synthesis processes, which can also introduce structural defects and impurities that degrade material performance over time. Unconventional techniques, including high-pressure methods, offer some improvements but typically require extended processing times, ranging from minutes to hours, and often lack the precision needed for fine control over material properties [16, 17]. In contrast, acoustic shock wave loading has emerged as a highly promising

---

*Address correspondence to this author at the Department of Mechanical Engineering, Keimyung University, Daegu 42601, Republic of Korea; E-mail: kimih@kmu.ac.kr & martinbritto@shctpt.edu

Received on 31-07-2025 Accepted on 01-09-2025 Published on 04-09-2025

alternative, operating on an ultra-short timescale from milliseconds to microseconds while enabling rapid energy transfer and controlled material transformation. This approach minimizes the time, significantly reduces the risk of defect formation or impurity incorporation. The ability to induce structural changes quickly and modify energy storage materials with enhanced performance characteristics. As such, this technique represents a growing area of interest, offering a novel pathway for overcoming the persistent limitations of conventional and high-pressure synthesis methods in the pursuit of next-generation energy storage solutions [18,19]. Few reports exist on how acoustic shock waves can enhance the electrochemical performance of materials through phase transitions, lattice compressions, and morphological transformations. Materials submitted to acoustic shock waves at transient pressures of about 2.0 MPa and with a temperature up to 864 K have undergone extensive structural and morphological changes. For instance, CdO nanorods experience morphological transformation from rod-shaped to honeycomb-like nanostructures, leading to an enhancement of surface area, ion diffusion, and redox activity. These changes result in a significant enhancement of specific capacitance and long-term cycling stability [20]. Multi-walled carbon nanotubes (MWCNTs) obtained improved electrochemical performances under shock-loaded conditions. Specific capacitance was enhanced through improved crystallinity, lowering electron scattering, and contact resistance. Shock-treated samples constituted ordered hexagonal networks, enabling improved ion diffusion and charge mobility. Even with increased scan rate, at 300 shock pulses sample still maintained 30% of its original capacitance, which indicates superior rate performance and electrolyte accessibility [21]. At 0.59 MPa pressure and 520 K temperature, acoustic shock wave applied to Bi_2Se_3 and CdSe. The CV analysis revealed that an increase in specific capacitance of both materials occurred with the increase in the number of shock pulses, with the maximum capacitance recorded after 400 shocks. EIS measurements showed a reduction in charge transfer resistance following shock treatment, and this indicates enhanced conductivity and ion transport. GCD curves showed longer charge-discharge times at 400 shock pulses [22]. Therefore, acoustic shock wave treatment is proving to be a promising approach for engineering high-performance electrode materials for energy storage devices.

Previous studies have primarily focused on the CdS structural, optical, and morphological behaviour under acoustic shock wave exposure, while limited attention has been given to its electrochemical performance. To address this research gap, the current research systematically investigates the acoustic shock wave exposure effect on the electrochemical behavior of shock-loaded CdS. The goal is to determine whether acoustic shock waves can induce beneficial modifications in the material’s physical and chemical properties to enhance its performance in energy storage applications.

In the earlier work, the effects of a series of acoustic shock pulses on CdS were characterized [23]. Among the tested samples, the 300 shock pulses exhibited significant morphological changes. This observation motivated a detailed analysis of that particular sample. The shock wave-induced morphological changes were found to correlate with changes in capacitance, potentially impacting the material’s suitability for electrochemical energy storage. Therefore, this study focuses on analyzing key performance metrics such as specific capacitance, charge transfer resistance, total capacitance, and conductivity to better understand how acoustic shock wave treatment influences the electrochemical properties of CdS. In addition to performance assessment, the research further seeks to discern what underlying mechanisms are behind any resultant improvement. In-depth morphological and surface studies will be performed to establish how acoustic shock waves affect properties like the surface roughness. Determining these effects is important for gaining insight into how mechanical energy at the micro level will improve electrochemical activity. Finally, the aim is to develop a new and efficient method for enhancing CdS's electrochemical functionality using acoustic shock wave treatment. This research has the potential to make significant additions to the general area of materials engineering and potentially provide new avenues for the optimization of electrochemically active materials by non-thermal energy-based methods.

SHOCK WAVE LOADING EXPERIMENT

Cadmium sulfide with a purity of 99.9% was obtained from SRL, India, and exposed to acoustic shock wave exposure without any further purification. A schematic representation of the semi-automatic Reddy tube arrangement is shown in Figure **1**. It comprises three parts: driver, driven, and diaphragm section. The movable sample holder was placed 10 mm away from the open end of the driver section. This open-end position also allows easy visual inspection of the status of the sample and removal of diaphragm fragments after each pulse, preventing blockage or contamination and enabling hundreds of uninterrupted shock wave exposures. A more detailed description of this setup is available in our previous work [23]. The sample was exposed to 300 shock pulses. To assess the impacts of exposure to a shock wave, CdS behaviour was

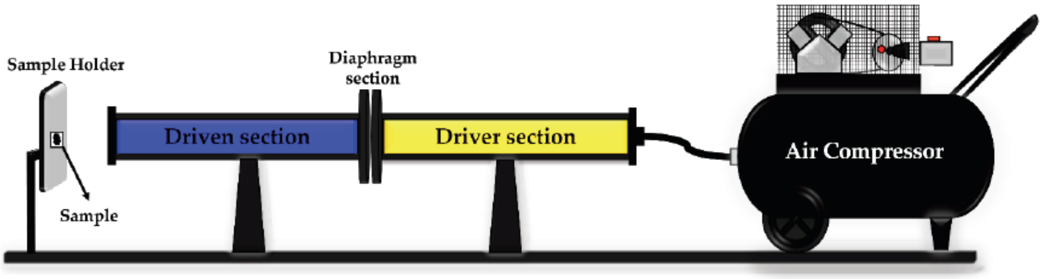

Figure 1: Schematic representation of the semi-automatic Reddy tube setup.

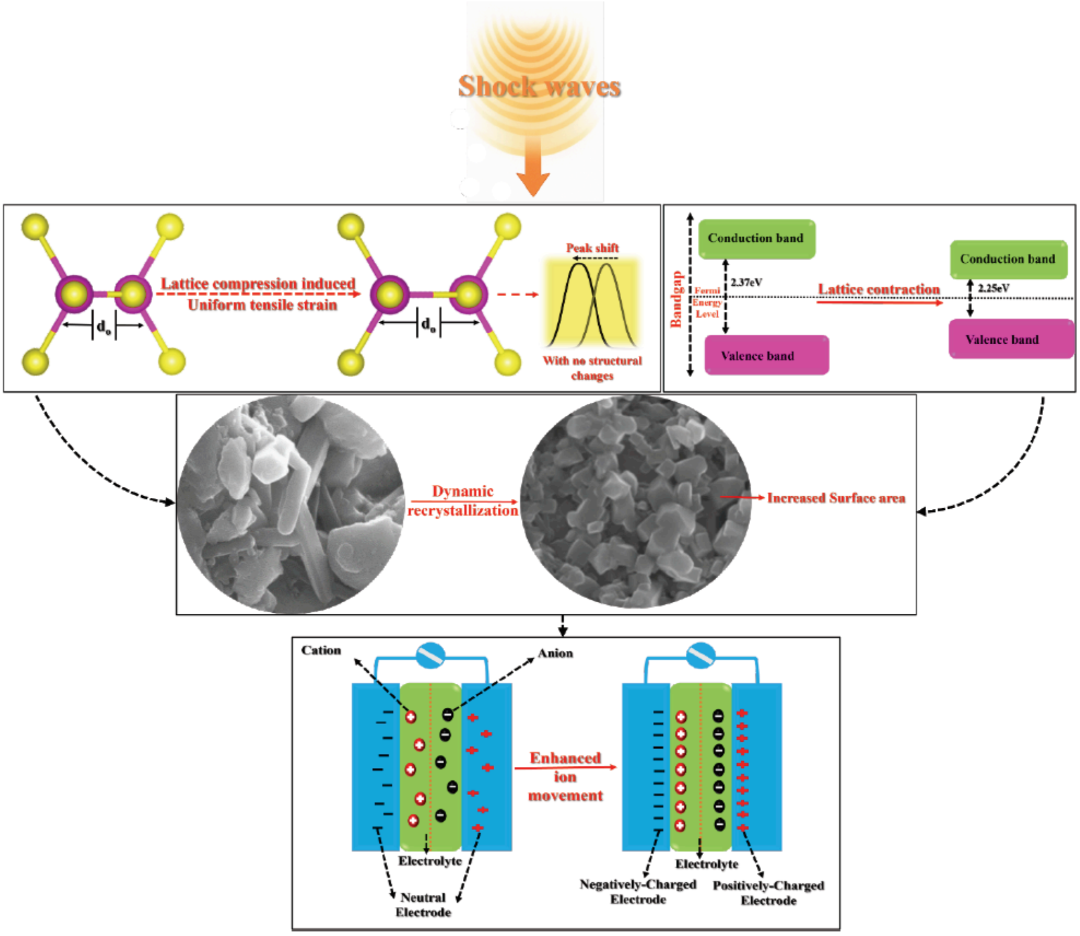

Figure 2: Schematic illustration of shock-wave-induced modifications in materials.

analyzed before and after shock wave treatment by various means, such as X-ray Diffraction (XRD), UV-Vis Diffuse Reflectance Spectroscopy (DRS), Field-Emission Scanning Electron Microscopy (FE-SEM), Brunauer-Emmett-Teller (BET), and Cyclic Voltammetry (CV). Figure **2** Schematic illustration of shock-wave-induced modifications in materials.

ANALYTICAL INSTRUMENTATION DETAILS

The X-ray diffraction (XRD) patterns of pristine CdS and CdS subjected to 300 shock pulses were obtained using a Bruker D2 Phaser powder diffractometer, employing CuKα$_1$ radiation (λ = 1.5406 Å). The 2θ scanning range was from 20° to 80° with a step of 0.02°. Rietveld refinement of the diffraction pattern was carried out on the FullProf suite from a single-phase hexagonal model (space group P63mc, ICSD #: 043599). UV-Vis DRS of pristine and 300 Shock pulses of CdS were recorded using a spectrophotometer (SHIMADZU UV-5600 PLUS), operating in the wavelength range between 185 and 3300 nm. Spectra were collected between 200 and 800 nm to explore changes in optical absorption behavior. FE-SEM of pristine and 300 Shock pulses of CdS was conducted using a SIGMA HV from Carl Zeiss, coupled with a Bruker Quantax 200-Z10 EDS system. The equipment worked with accelerating voltages between 200 V to 30 kV and magnification powers from 20x up to 1,000,000x. The instrument offered a resolution of 1.0

nm at an accelerating voltage of 30 kV and 3 nm at 1 kV, while the probe current capacity exceeded 100 nA. BET analysis was performed using an instrument, the Belshorp Max, Model No. BELSORP-max, manufactured by MicrotracBEL Corp., Japan. It operates using nitrogen (N_2) gas under the condition of liquid nitrogen at 77 K, with a measurement resolution starting from $P/P_0 \approx 10^{-6}$. The Cyclic voltammetry (CV) profile of pristine and 300 Shock pulses of CdS was obtained with the Princeton Applied Research Versa STAT MC system. The equipment has a large frequency range (1 Hz to 1 MHz), and it can be used successfully for electrochemical characterization of solid-state as well as liquid-phase samples. Electrochemical measurements were carried out using a three-electrode configuration. CdS samples served as the working electrode, and a saturated calomel electrode (SCE) was used. The measurements were conducted in an aqueous electrolyte solution, typically 1 M KOH, to evaluate the electrochemical performance.

X-RAY DIFFRACTION (XRD) ANALYSIS

Figure **3** shows the XRD pattern of pristine and 300-shock-pulsed CdS, along with the standard pattern. The diffraction pattern obtained corresponds closely with the standard reference data provided in the JCPDS card no. 89-2944, verifying the crystalline nature of the sample. The material exhibits a hexagonal crystal system and belongs to the $P6_3mc$ space group, which features symmetry elements such as mirror planes and glide planes, ensuring structural regularity. The atomic configuration follows a typical wurtzite-type structure, commonly seen in II–VI semiconductors, where Cd and S atoms are arranged in a tetrahedral coordination. Tetrahedrally coordinated each Cd atom with four S atoms, and conversely, each S atom bonded to four Cd atoms, creating a strong covalent framework. This network is stacked along the c-axis, primarily held together by weak van der Waals interactions, resulting in a layered structure with an ABABAB stacking pattern. The determined lattice constants are a = b = 4.14 Å and c = 6.71 Å, and its unit cell volume is 99.67 $Å^3$. This orderly stacking arrangement contributes to the uniform distribution of atoms and enhances the crystal's structural stability. The identified crystal structure is consistent with previously reported results in the literature [24, 25].

The material maintains its hexagonal crystal structure even after being subjected to 300 shock pulses. However, slight shifts in diffraction peaks toward lower angles were noted for the (100), (002), and (101) planes under this condition. Figure **3**(**b**) presents a magnified view of these specific planes. The applied shock waves result in rapid compression, which can cause temporary lattice deformation. According to the material's behavior under extreme conditions, this deformation may be followed by either relaxation or rapid expansion. These dynamics can modify the atomic arrangement within the crystal, impacting its structural integrity [26, 27]. Moreover, the introduction of uniform tensile strain perpendicular to certain directions can further distort the lattice, affecting atomic spacing and inducing mechanical stress. This leads to changes in the interplanar distance (d-spacing), which in turn shifts X-ray diffraction peaks to lower angles. These angular shifts are indicative of strain-related lattice changes and provide valuable information on the degree of deformation caused by shock wave pulsus [28].

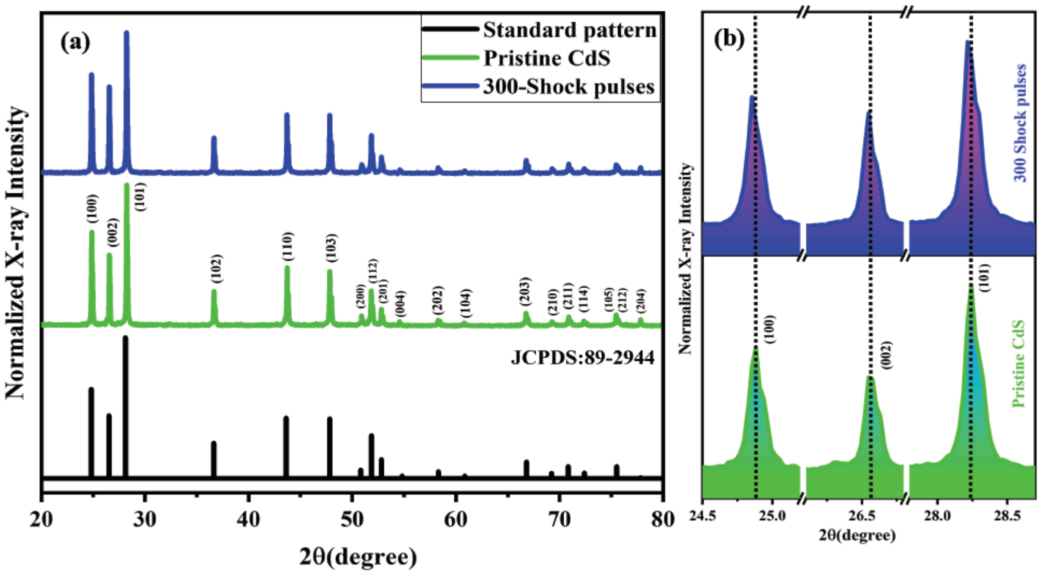

Figure 3: XRD pattern (**a**) pristine and 300 shock pulses of CdS with the standard pattern (**b**) magnified view of (100), (002), and (101) planes.

UV-VIS DIFFUSE REFLECTANCE SPECTROSCOPY (DRS)

Figure **4** shows the reflectance spectra of pristine and 300 shock pulses of CdS. At 300 shock-loaded condition, CdS optical properties were modified. The bandgap was calculated by using the Kubelka-Munk equation, which helps to understand the optical properties of the material.

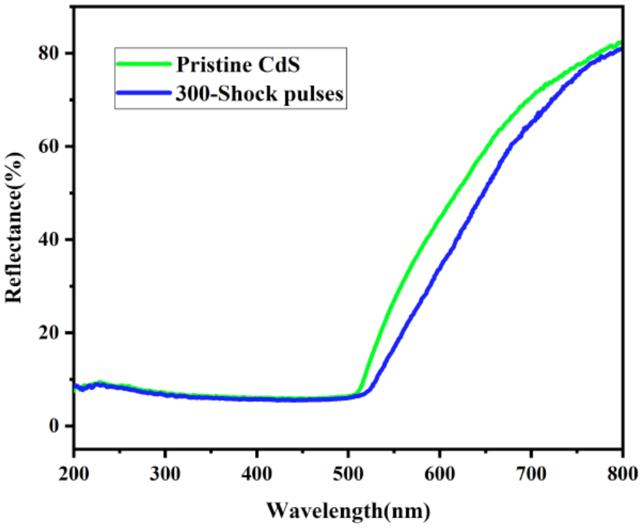

Figure 4: Reflectance spectra of pristine and 300 shock pulses of CdS.

The optical bandgap can be precisely estimated by correlating reflectance data with absorption characteristics using the relation $(F(R)h\upsilon)^2=A(h\upsilon-Eg)$. In this expression, $F(R_\infty)$ denotes the K-M function, which can also be known as the remission function, whereas R_∞ stands for the diffuse reflectance. The term A is a constant associated with transition probability, and the diffuse reflectance R_∞, hv refers energy of the photon, and Eg represents the bandgap [30]. Figure **5** illustrates the K-M plot of pristine CdS and 300 Shock pulses. The plots are constructed by graphing $(F(R_\infty)h\upsilon)^{2,}$ and hv linear fittings are used to the present experimental data to analyze the optical transition characteristics. The bandgap energy is determined by extrapolating the fitted lines to the x-axis (photon energy axis), where the intersection indicates the material's bandgap. This method provides a reliable and accurate determination of bandgap values.

CdS demonstrated a bandgap of 2.37 eV initially, which is consistent with the literature values of CdS [31]. At 300 shock pulses, a reduction in the bandgap was observed; the bandgap dropped to 2.25 eV, which is still well aligned with literature values of CdS [32]. This change indicates a significant modification in the optical behavior of the material. The impact of shock wave-induced rapid compression, a crystal lattice leads to lattice contraction or expansion, which leads to lattice deformation. These structural changes displace atoms from their equilibrium positions, causing distortions that influence the material's electronic structure, including its bandgap [33]. When the lattice contracts, interatomic distances decrease, leading to reduced lattice constants and enhanced overlap of electronic orbitals [34, 35]. This increased orbital interaction typically lowers the conduction band and raises the valence band, thereby decreasing the energy required for electron excitation and effectively narrowing the bandgap.

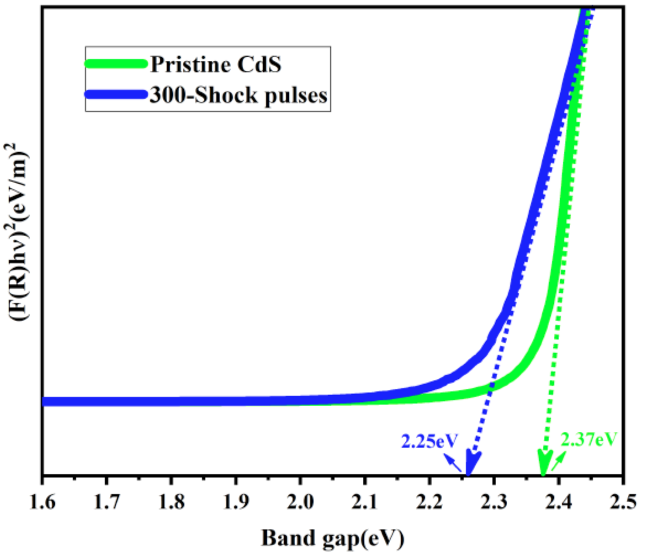

Figure 5: Kubelka-Munk plot of pristine and 300 shock pulses of CdS.

FIELD EMISSION SCANNING ELECTRON MICROSCOPY (FESEM)

Figure **6** shows the FE-SEM images of pristine and 300 shock pulses of CdS The pristine CdS exhibits a rod-shaped structure, suggesting that the crystal growth proceeds in an anisotropic manner [36]. Upon applying 300 shock pulses, the morphology transitions from rod-like to a more cube-like shape. This transformation is attributed to dynamic recrystallization induced by shock waves [37]. At 300 shock pulses, the material is at a critical energy level. Because of its low thermal conductivity, heat builds up locally and leads to localized intense heating, resulting in dynamic recrystallization and a momentary molten condition. This is followed by the fragmentation and reorganization of rod-shaped particles into a cube-like structure. The deformation was created by shock waves, induced thermal softening, high-speed resolidification, and fragmentation caused by the combined effects of 0.59 MPa pressure and 520 K temperature, which induces superheating following supercooling effects that occur within milliseconds. Localized heating induces a premelting process,

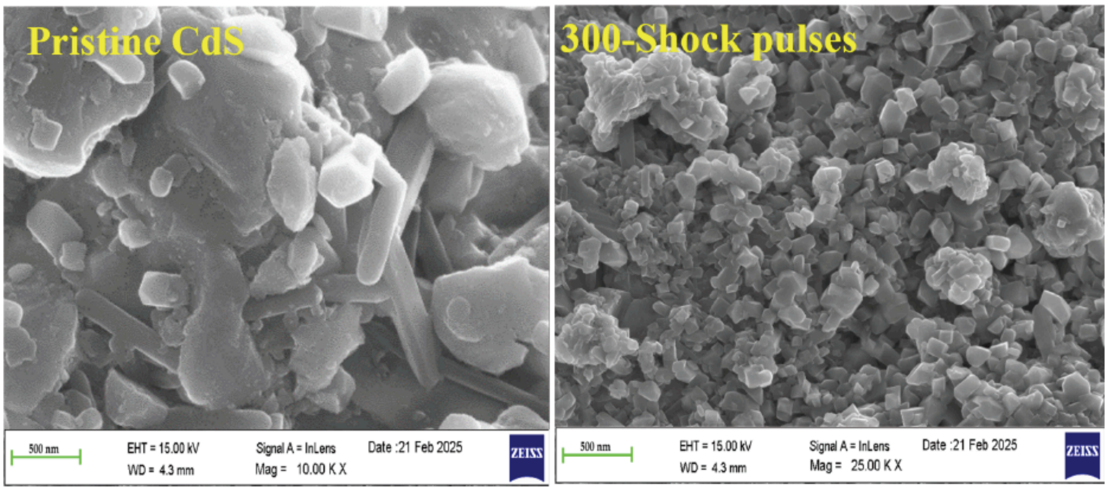

Figure 6: FE-SEM images of pristine and 300 shock pulses of CdS, along with their respective 2D surface profiles.

producing temporary molten areas that quickly resolidify, creating new grain boundaries and more dense, stable material. The cube-like morphology is a result of localized melting and the quick resolidification induced by restricted heat dissipation at 300 shock pulses [38]. Pristine CdS exhibits a rod-like morphology, which leads to a relatively low surface area, and thus, electroactive sites will be limited. After 300 shock pulses, the particles become more fragmented, uniformly dispersed, and adopt a cube-like morphology with smaller sizes along with rougher surfaces. This morphology transformation from rod to cube significantly increases the surface area, which in turn enhances the electrode-electrolyte interface. The increased surface area creates more active sites for ion adsorption and which facilitates ion transport, thereby leading to improved ion diffusion kinetics. This augmentation directly contributes to a higher specific capacitance by enabling more efficient charge storage and faster electrochemical response [39].

BRUNAUER-EMMETT-TELLER (BET) ANALYSIS

Figure **7** illustrates the surface area and pore distribution of the CdS sample with the corresponding Barrett-Joyner-Halenda (BJH) pore size distribution plot, inset a) Pristine and b) 300 Shock pulses. The nitrogen adsorption-desorption isotherms and pore size distribution curves reveal that both pristine and 300-shock pulse CdS exhibit mesoporous characteristics, indicated by type IV isotherms with H3 hysteresis loops it as confirmed by the Barrett-Joyner-Halenda (BJH) plot [40,41]. Pristine CdS shows a BET surface area of 1.07 m^2/g and an average pore diameter of 19.701 nm, while 300 shock pulses display an increased surface area of 2.10 m^2/g and a reduced pore diameter of 9.4977 nm, both within the mesoporous range (2-50 nm). The enhanced surface area and reduced pore diameter indicate improved ion diffusion and electrolyte access. These textural enhancements play a vital role and significantly impact electrochemical performance, particularly in

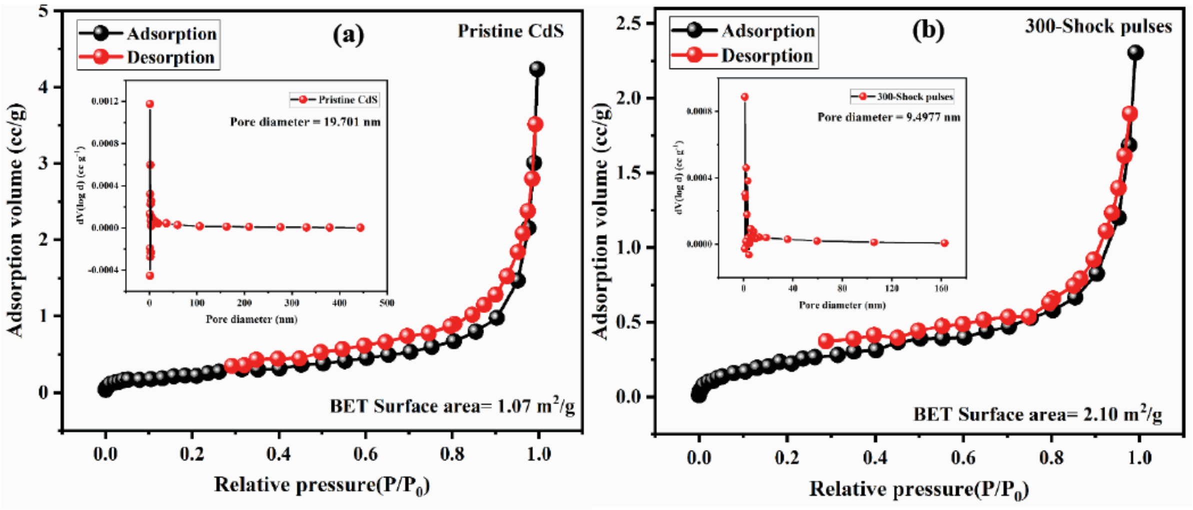

Figure 7: BET surface area and pore distribution of CdS along with the corresponding Barrett-Joyner-Halenda (BJH) pore size distribution plot, inset **a**) Pristine and **b**) 300 Shock pulses.

supercapacitor applications. The shock wave-treated CdS exhibits a higher specific capacitance compared to pristine CdS, due to its higher active surface area and superior charge storage ability. Reduced mesoporosity allows for quicker charge-discharge cycles and enhances the energy storage. Furthermore, the BET analysis was well correlated with the FE-SEM images of pristine and 300 shock pulses of CdS. Thus, the shock wave treatment not only modifies the structural properties but also enhances the electrochemical behavior, making the material more suitable for energy storage devices.

CYCLIC VOLTAMMETRY (CV) ANALYSIS

Figure **8** shows the CV curve of a pristine and 300 shock pulses exposed CdS sample studied using CV measurements in 1M KOH electrolyte, using a standard calomel electrode as the reference and platinum as the counter electrode. It is scanned at different scanning rates - as 5, 10, 25, 50,75, and 100 mVs^{-1}, within the potential range from 0 to 0.5 (V). The obtained CV curves for both pristine and 300 shock pulses of CdS represent distinct cathodic-anodic peaks, revealing the pseudocapacitive behavior of CdS in the KOH electrolyte [42]. The specific capacitance of pristine and 300 shock pulses of CdS was calculated for different scanning using the following expression,

$$Cp = \frac{1}{\mathrm{Vm}(\mathrm{V}-V_0)}\int_{v_0}^{v} I(\mathrm{v})\mathrm{dv}\ldots\ldots\ \mathrm{Fg}^{-1}$$

While Cp is the specific capacitance, V is used for the scan rate, m for the mass of the material utilized, (V-V$_0$) for the potential difference, and $\int_{v_0}^{v} I(\mathrm{v})\mathrm{dv}$ is the hysteresis loop area. For pristine CdS, the obtained specific capacitance values are 266, 231, 184, 155, 139, and 128 F g^{-1} at different scan rates of 5, 10, 25, 50, 75, and 100 mVs^{-1}, respectively. By applying 300 shock pulses, the specific capacitances tend to increase, such as 268, 234, 193, 167, 152, and 142 Fg^{-1} at the corresponding scan rates, indicating that CdS obtained improved electrochemical performance by shock wave exposure. The specific capacitance decreases as the scan rate increases. With increasing scan rate, the contribution from the diffusive mechanism decreases due to the rapid movement of charges across the material, which leads to a reduction in the time which is available for ions to diffuse into the active material lattices. Therefore, the capacitive process is the major source of the total CV current response. Figure **9** shows the specific capacitance of pristine and 300 shock pulses of CdS for different scan rates. A bandgap is vital for improving their electrochemical performance, especially in supercapacitor fields of application where high specific capacitance is needed. The bandgap of any material can be described as the energy gap between its valence band and conduction band; a smaller bandgap indicates lower energy needed to activate electrons from the valence band to the conduction band. This lower energy level greatly enhances its conductivity by allowing easier passage of charge carriers (electrons and holes). Enhanced conductivity guarantees better charging and discharging of charges in electrochemical processes with greater speed, thus enhancing the capability of the electrode to store and release energy quickly. In addition, a smaller bandgap usually means that there are more electronic states in the band structure, such as defect levels or mid-gap states, that may act as additional active sites for electrochemical reactions. These active sites allow more ions of the electrolyte to be engaged with the electrode surface, raising the charge storage capacity and hence the specific capacitance [43]. For pristine CdS, a bandgap was found to be 2.37 eV; for 300 shock pulses, the bandgap decreased to 2.25 eV. The shock wave treated CdS, thereby increasing its electrical conductivity and improving the ion transport channels. Lower bandgap materials tend to exhibit enhanced surface chemistry, as well as a greater concentration of electronic states at the Fermi level, which further improves the double-layer capacitance and pseudocapacitive behavior. The measured decrease in the bandgap of CdS upon shock wave treatment is

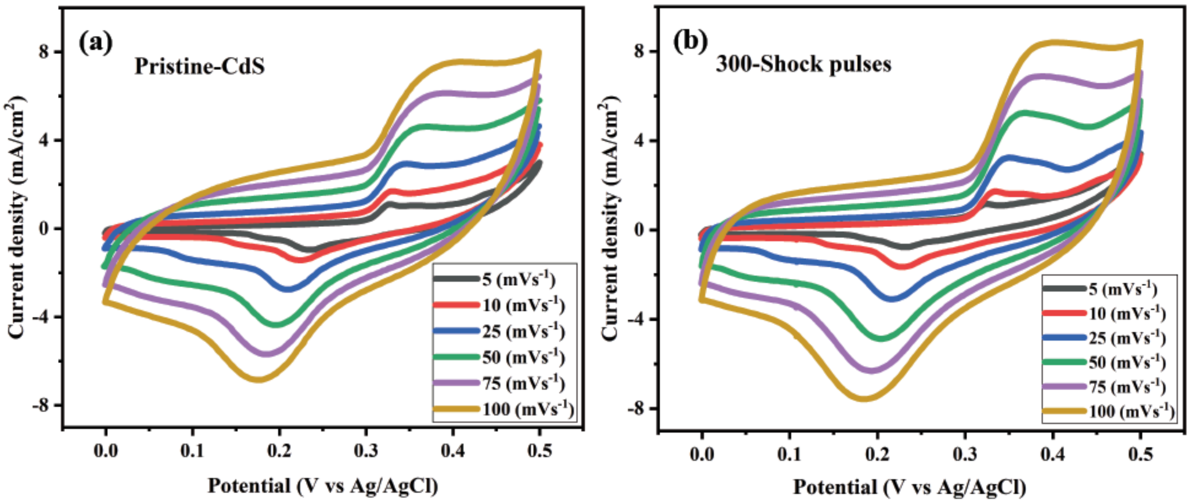

Figure 8: CV Curve of CdS (**a**) Pristine (**b**) 300 shock pulses exposed.

accompanied by an increase in its specific capacitance, which shows a clear inverse correlation between bandgap and electrochemical performance. This further emphasizes the need to engineer the electronic structure of electrode materials toward improved supercapacitor performance.

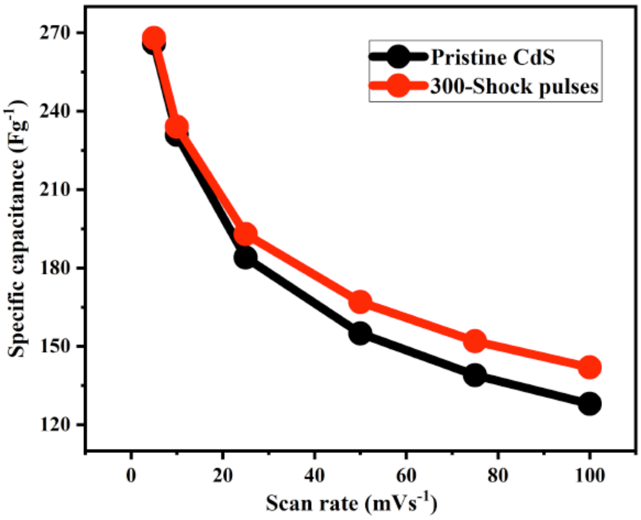

Figure 9: Specific capacitance of pristine and 300 shock pulse-exposed CdS.

The current response of a material observed in cyclic voltammetry (CV) can be due to two main mechanisms: a capacitive current contribution and a slow diffusion-controlled process. These two contributions can be distinguished based on the power law relationship between current (i) and scan rate (v), which is generally written as [44],

$$i = av^{b}$$

In this equation, the exponent b gives information about the prevailing charge storage mechanism. A b-value around 0.5 is typical for a diffusion-controlled process, while a b-value close to 1.0 indicates a capacitive behavior. The b-values for pristine and 300 shock pulses of CdS were obtained by plotting the logarithm of the peak current against the logarithm of the scan rate for both anodic and cathodic processes, as shown in Figure **10**(**a**). For pristine CdS, the anodic and cathodic b-values were found to be 0.60 and 0.92, respectively. The high cathodic b-value indicates a dominant capacitive-controlled charge storage mechanism. After applying 300 shock pulses, the anodic b-value remains unchanged at 0.60. In contrast, the cathodic b-value slightly decreases to 0.89, as shown in Figure **10**(**b**). Despite the slight decrease, the cathodic process continues to display strong capacitive behavior. This indicates that pristine and 300 shock pulses of CdS have surface-controlled kinetics, and the shocked sample retains a high capacitive contribution, potentially owing to structural or surface activation caused by the mechanical pulses. In addition, the relative contribution of capacitive and diffusion-controlled mechanisms was quantitatively examined based on the Dunn method by applying the following equation [45],

$$i = k_1v + k_2v^{½}$$

Here, k_1 and k_2 are constants, evaluated from the slope and intercept of a linear plot of $i(V)/v^{1/2}$ versus $v^{1/2}$, respectively, and v is the scan rate. Figure **11**(**a**) and (**b**) show that the capacitive and diffusion-controlled charge storage contributions of the pristine and 300 shock-pulsed CdS were quantitatively determined at 5 mVs^{-1}. The CV current response at 5 mV s^{-1} of the material CdS is calculated. Based on the analysis, the charge storage is dominated by a high percentage of capacitive behavior. For the pristine CdS, the capacitive contribution is 75%, while for the 300 shock pulses, it increases to 78%. Figure **11**(**c**) and (**d**) show that the capacitive and diffusion-controlled charge storage contributions of the pristine and 300 shock-pulsed CdS were quantitatively determined at

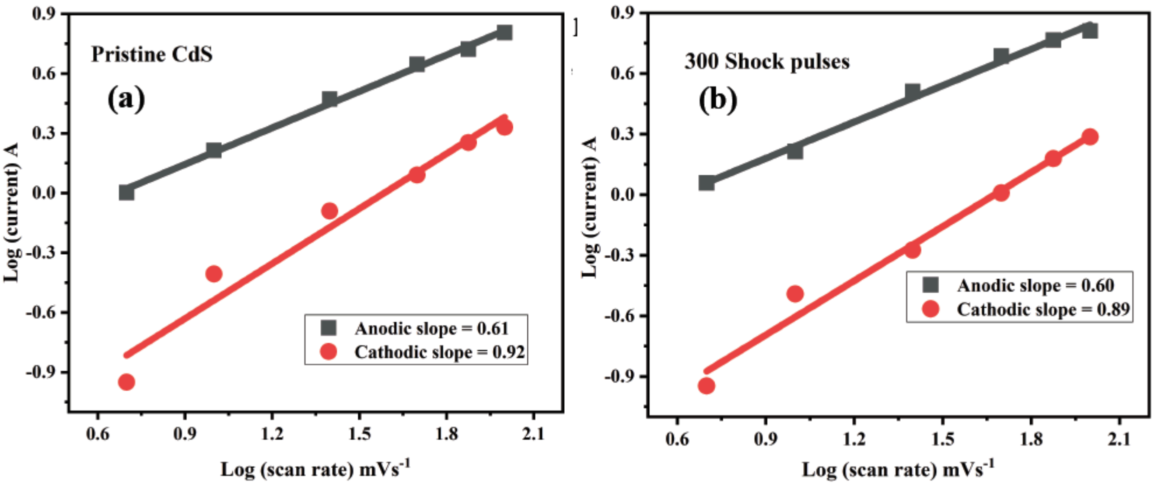

Figure 10: Calculated b-values of CdS (**a**) Pristine and (**b**) 300 Shock pulses.

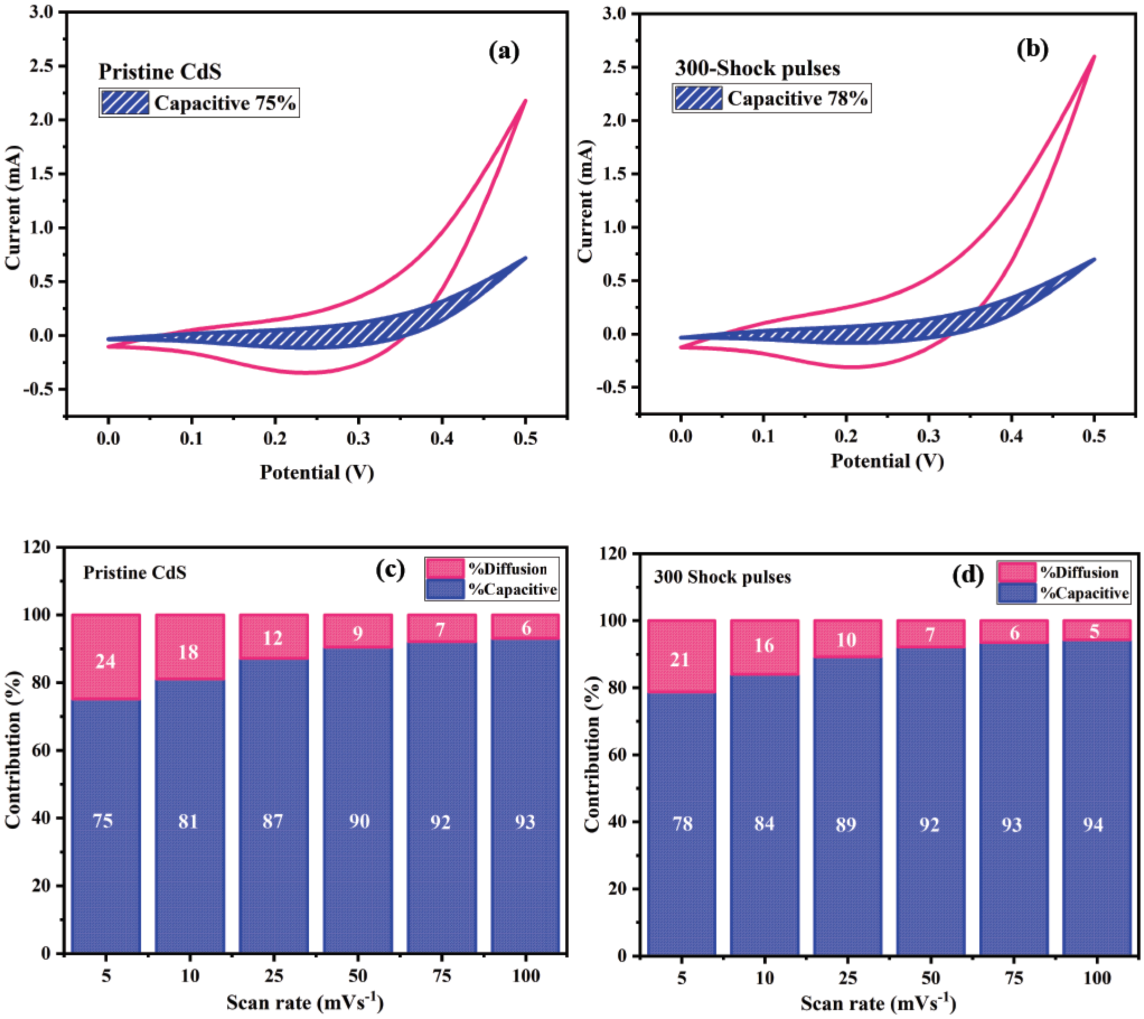

Figure 11: Capacitive-Diffusive contribution of (**a**) Pristine CdS and (**b**) 300 Shock pulses at 5 mVs^{-1}, and Capacitive-Diffusive contribution of (**c**) Pristine CdS and (**f**) 300 Shock pulses at different scan rates.

different scan rates. In the case of the pristine CdS, the capacitive contribution rises from 75% at 5 mV s^{-1} to 93% at 100 mV s^{-1}, while the corresponding diffusion-controlled contribution drops from 24% to 6%. For comparison, the sample subjected to 300 shock pulses shows a greater capacitive contribution at all scan rates, from 78% at 5 mV s^{-1} to 94% at 100 mV s^{-1}, with a corresponding decrease in diffusion-controlled contribution from 21% to 5%. This increase in capacitive behavior is an indication that the shock pulses have significantly enhanced the surface kinetics and electrochemical accessibility of the CdS. The shock wave treatment is likely to cause microstructural modifications in the form of higher surface area, defects, or enhanced conductivity, which contribute towards faster surface redox reactions. Consequently, the charge storage becomes more dominated by surface-controlled mechanisms, and the dependence on slower ion diffusion into the bulk is reduced. These results show that acoustic shock wave treatment is a powerful approach to tuning the charge storage mechanism and improving the pseudocapacitive performance of CdS-based electrodes [46].

GALVANOSTATIC CHARGE-DISCHARGE (GCD) ANALYSIS

Figure **12** represents the GCD curve of pristine and 300 shock pulses of CdS. The galvanostatic charge-discharge (GCD) response was investigated to analyze the major capacitance parameters, such as specific capacitance, specific power, and specific energy, at different current densities. GCD analysis is more of a stable method compared to cyclic voltammetry (CV) measurements in determining specific capacitance [47]. The specific capacitances of pristine and 300 shock pulses of CdS are calculated by using the following equation,

$$\mathrm{Csp} = \frac{I\Delta t}{m\Delta V}$$

Whereas, I signify the current (A), m is the electrode material weight (g), and ΔV signifies the used voltage (V) [48]. Pristine CdS exhibited specific capacitance values of 316, 308, 300, 288, and 200 Fg^{-1} at different specific currents of 2, 4, 6, 8, and 10 Ag^{-1}, respectively, with a retention of 63.3% from 10 to 2 Ag^{-1}. For 300

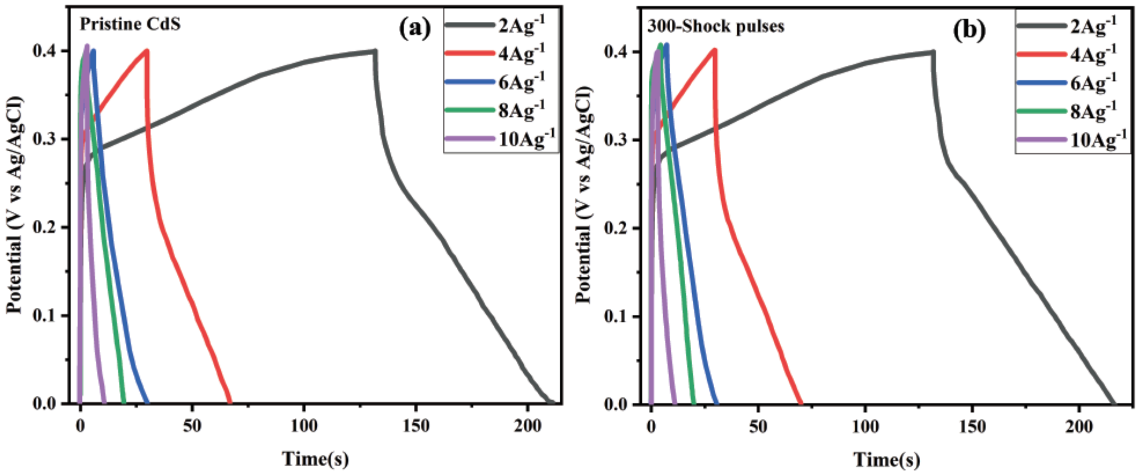

Figure 12: GCD curve of CdS (**a**) Pristine (**b**) 300 shock pulses.

shock pulses, exhibited specific capacitance values of 336, 320, 312, 304, and 240 Fg^{-1} at different specific currents of 2, 4, 6, 8, and 10 Ag^{-1}, respectively, with a retention of 71.4% from 10 to 2 Ag^{-1}. Figure **13** Variation of Specific capacitance (Fg^{-1}) versus specific current (Ag^{-1}) of pristine and 300 shock pulses of CdS. As current density increases, the specific capacitance of both samples reduces. This is primarily because of the short period for ions to diffuse within the electrode material and move to electroactive sites at higher current densities, decreasing charge storage efficiency. At lower current densities, ions are given sufficient time to access these sites, leading to greater capacitance. Under shock-loaded conditions, CdS exhibits enhanced capacitance at all current densities, which can be due to increased surface area and decreased pore size. These changes facilitate ion transport and surface reactivity and thus enhance electrochemical performance in general [49,50]. The cyclic stability increased from 63.3% to 71.4%, reflecting better energy storage behavior of the charge at increased current densities resulting from enhanced ion diffusion and decreased resistance upon shock wave treatment. Shock wave application seems to increase the electrochemical performance of the material through enhancing more active surface area and reducing internal resistance, which work synergistically to facilitate accelerated ion diffusion and improved charge storage. The enhancement of the specific capacitance after shock wave treatment points towards enhanced electrochemical response of the material and further optimization potential in supercapacitor applications. The GCD profiles also indicate an increased IR drop and longer discharge times, which are a testament to improved electrochemical kinetics, increased capacitance, and stable cycling behavior, establishing CdS as a viable material for high-performance supercapacitor systems.

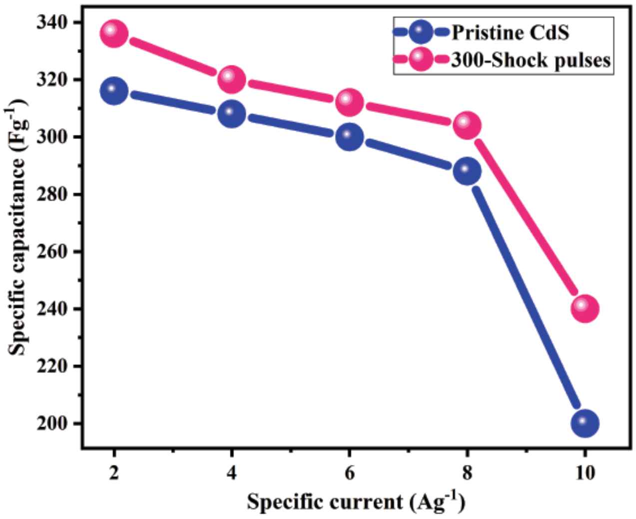

Figure 13: Variation of Specific capacitance (Fg^{-1}) versus specific current (Ag^{-1}) of pristine and 300 shock pulses exposed CdS.

ELECTROCHEMICAL IMPEDANCE SPECTROSCOPY (EIS) ANALYSIS

Figure **14** represents the Nyquist plot of pristine and 300 shock pulses of CdS, along with the corresponding equivalent circuit inset. The Nyquist plot is plotted between the real component impedance (Z') on the x-axis and the imaginary component impedance (Z'') on the y-axis. For pristine CdS, a large semicircle was observed in the region known as the higher frequency region [51]; the large semicircle arc, typically present in the higher frequency region, decreased after 300 shock pulses. Shock wave-induced thermal energy reduces the semicircle in Nyquist plots due to increased electrical contact between particles and a decrease in interparticle or interface resistance. This is because shock wave-induced thermal energy-driven dynamic recrystallization favors increased particle-particle connectivity through the rearrangement of grain boundaries, which enhances charge transport paths. Consequently, the total resistance related to interfaces or grain boundaries is minimized, resulting in a smaller semicircle in electrochemical impedance spectroscopy [52]. The equivalent circuit in Figure **14** comprises a capacitor (C) in parallel with a series of two resistors (R_1 and R_2) and an inductor (L). This is the circuit that simulates the electrical behavior of the system, with R_1 and R_2 being different resistive contributions and L being inductive effects. ZSimpWin (version 3.20) software was used to fit and determine resistance values. The bulk resistance and bulk capacitance were obtained from the ZSimpWin software, and the bulk conductivity (σ) for the grain for pristine and 300 shock pulses of CdS was determined by using the following formula:

$$\sigma = d / (RgA)$$

where d is the thickness of the sample, Rg is the bulk resistance, and A is the area of the electrode. The findings validate that resistance drops following exposure to shock waves, which consequently enhances capacitance and conductivity. Table **1** illustrates the calculated grain bulk resistance (Rg), bulk capacitance (Cg), and bulk conductivity (σ_g). As Table **1** shows that the bulk resistance of pristine is found to be 6.613×10^3 after 300 shock pulses, significantly decreasing to 1.262×10^3, reflecting a marked improvement (more than 5 times) in electrical conductivity. This drop in resistance corresponds to a substantial increase in bulk conductivity was observed for pristine and 300 shock pulses, rising from 1.51×10^{-4} to 7.92×10^{-4}. In addition, the bulk capacitance also increased from 7.9026×10^{-6} F to 9.807×10^{-6} F, representing improved dielectric properties, probably because of microstructural changes like elevated grain boundary mobility or enhanced polarization capability. Overall, the results validate that acoustic shock wave treatment significantly enhances the efficiency of charge transport and boosts the capacity of the material for energy storage and transmitting electrical charge.

CONCLUSION

This study demonstrates the effectiveness of acoustic shock wave treatment as a novel and scalable method for enhancing the structural, optical and electrochemical properties of electrode materials for supercapacitor applications. Structural analyses revealed peak shifts in XRD without phase degradation, bandgap narrowing from 2.37 to 2.25 eV, and a morphology transformation from rod- to cube-like shapes. The increase in surface area from 1.07 to 2.10 m^2/g and the reduction in average pore diameter from 19.70 to 9.50 nm improved ion transport and surface reactivity. These physical changes translated directly into electrochemical benefits. Specific capacitance increased across all scan rates, with notable

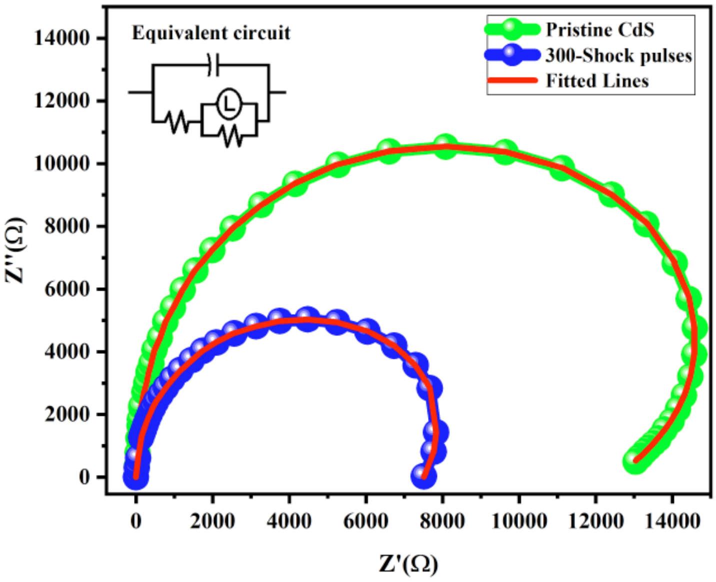

Figure 14: Nyquist plot of pristine and 300 shock pulses of CdS along with the corresponding equivalent circuit inset.

Table 1: Comparison of grain bulk resistance (Rg), bulk capacitance (Cg), and bulk conductivity (σ_g) of pristine and 300 shock pulses of CdS

Sample	Bulk Resistance-R_g (Ω.cm)	Bulk Capacitance-C_g (F)	Bulk Conductivity- σ_g (W m^{-1} K^{-1})
Pristine CdS	6.613×10^3	7.9026×10^{-6}	1.51×10^{-4}
300-Shock pulses	1.262×10^3	9.807×10^{-6}	7.92×10^{-4}

improvements under shock-loaded conditions. Under shock loaded condition capacitive contribution increased from 75% to 78% at 5 mV s-1 and 93% to 94% at 100 mV s-1 indicating a stronger surface-controlled charge storage mechanism. Enhanced cycling stability was also observed, with capacitance retention improving from 63.3% to 71.4%. Furthermore, after exposure to 300 shock pulses, the sample exhibited a substantial decrease in bulk resistance from 6.613×10^3 to 1.262×10^3 Ω.cm along with a significant increase in bulk conductivity from 1.51×10^{-4} to 7.92×10^{-4} W m^{-1} K^{-1} and an enhancement in bulk capacitance from 7.90×10^{-6} to 9.81×10^{-6} F. These improvements facilitate faster charge transport, reduced energy loss, and better dielectric behavior, collectively contributing to enhanced overall electrochemical performance and energy storage efficiency. The scope of this work highlights the utility of acoustic shock waves as a clean, rapid, and energy-efficient processing technique capable of inducing beneficial microstructural and electronic changes without chemical modification or high-temperature processing. This approach not only improves the fundamental performance metrics critical to supercapacitor operation, such as capacitance, conductivity, and stability, but also offers a scalable route to enhance the efficiency of electrode materials. The findings underscore the broader potential of acoustic shock wave engineering in next-generation energy storage technologies where performance, scalability, and process simplicity are key.

DATA AVAILABILITY STATEMENT

The supporting data are available from the corresponding author upon reasonable request.

CREDIT AUTHORSHIP CONTRIBUTION STATEMENT

F. I.M.B. - Methodology, Investigation, Data curation, Writing-original draft, Writing and editing, S. O- Formal analysis, S. A. M. B. D- Conceptualization, Supervision, Investigation, writing review and editing, I. K - Formal analysis. All the authors discussed the results and commented on the manuscript.

DECLARATION OF COMPETING INTEREST

The authors declare that they have no known competing financial interests or personal relationships that could have appeared to influence the work reported in this paper.

CONFLICT OF INTEREST

The authors declare no conflict of interest regarding the publication of this paper.

ACKNOWLEDGMENT

The authors would like to thank TNSCST for their support through the RFRS scheme (TNSCST-13301/RFRS/PS/VM/2023-2024) and Sacred Heart College (Autonomous) for the Abraham Panampara Research Fellowship (APRF/06/2022/03). This research was supported by the Brain Pool program, funded through the National Research Foundation of Korea (RS-2023-00219593).

REFERENCES

[1] Li J, Chen S, Zhu X, *et al.* Toward Aerogel Electrodes of Superior Rate Performance in Supercapacitors through Engineered Hollow Nanoparticles of $NiCo_2O_4$. Adv. Sci, 2017; 4: 1-8. https://doi.org/10.1002/advs.201700345

[2] Liu Y, Wen S, Shi W Co_3S_4 nanoneedles decorated on $NiCo_2O_4$ nanosheets for high-performance asymmetric supercapacitors, Mater. Lett, 2018; 214: 194-197. https://doi.org/10.1016/j.matlet.2017.12.014

[3] Bhagwan J, Nagaraju G, Ramulu B, *et al.* Rapid synthesis of hexagonal $NiCo_2O_4$ nanostructures for high-performance asymmetric supercapacitors. Electrochim. Acta, 2019; 299: 509-517. https://doi.org/10.1016/j.electacta.2018.12.174

[4] Huang Y, Miao YE, Lu H, *et al.* Hierarchical $ZnCo_2O_4{}^{@}NiCo_2O_4$ core-sheath nanowires: Bifunctionality towards high-performance supercapacitors and the oxygen-reduction reaction. Chem. - A Eur. J., 2015; 21: 10100-10108. https://doi.org/10.1002/chem.201500924

[5] Chang JK, Lin CT, Tsai WT. Manganese oxide/carbon composite electrodes for electrochemical capacitors. Electrochem. Commun., 2004; 6: 666-671. https://doi.org/10.1016/j.elecom.2004.04.020

[6] Toupin M, Belanger D, Hill IR, *et al.* Performance of experimental carbon blacks in aqueous supercapacitors. J. Power Sources, 2005; 140: 203-210. https://doi.org/10.1016/j.jpowsour.2004.08.014

[7] Naudin E, Ho HA, Branchaud S, *et al.* Electrochemical polymerization and characterization of poly(3-(4-fluorophenyl) thiophene) in pure ionic liquids. J. Phys. Chem. B, 2002; 106: 10585-10593. https://doi.org/10.1021/jp020770s

[8] Prasad KR, Koga K, Miura N. Electrochemical deposition of nanostructured indium oxide: high-performance electrode material for redox supercapacitors. Chem. Mater., 2004; 16: 1845-1847. https://doi.org/10.1021/cm0497576

[9] Gao P, Liu J, Zhang T. Hierarchical TiO_2/CdS “spindle-like” composite with high photodegradation and antibacterial capability under visible light irradiation. J. Hazard. Mater., 2012; 229: 209-216. https://doi.org/10.1016/j.jhazmat.2012.05.099

[10] Zhang K, Liu X, Sun Y. Synthesis and electrochemical properties of $LiFePO_4$/C composite cathode material prepared by a new route using supercritical carbon dioxide as a solvent. J. Mater. Chem., 2011; 46: 6975-6980. https://doi.org/10.1039/c1jm10168d

[11] Moore VC, Strano MS, Haroz EH. Individually suspended single-walled carbon nanotubes in various surfactants. Nano Lett., 2003; 3: 1379-1382. https://doi.org/10.1021/nl034524j

[12] Jie JS, Zhang WJ, Jiang Y. Photoconductive characteristics of single-crystal CdS nanoribbons. Nano Lett., 2006; 6: 1887-1892. https://doi.org/10.1021/nl060867g

[13] Li Q, Guo B, Yu J. Highly efficient visible-light-driven photocatalytic hydrogen production of CdS-cluster-decorated

graphene nanosheets. Am. Chem. Soc., 2011; 133: 10878-10884. https://doi.org/10.1021/ja2025454

[14] Pawar SA, Patil DS, Shin JC, *et al.* Enhanced battery-type supercapacitor performance based on composite structure of nickel cobaltite and cadmium sulfide. J. Electroanal. Chem., 2020; 873: 114370. https://doi.org/10.1016/j.jelechem.2020.114370

[15] Dong R, Ye Q, Kuang L, *et al.* Enhanced supercapacitor performance of Mn_3O_4 nanocrystals by doping transition metal ions. ACS Appl. Mater. Interfaces, 2013; 5: 9508-9516. https://doi.org/10.1021/am402257y

[16] Sivakumar A, Lidong D, Sahaya Jude D S, *et al.* Acoustic shock wave-induced short-range ordered graphitic domains in amorphous carbon nanoparticles and correlation between magnetic response and local atomic structures. Diamond Relat. Mater. 2024; 141: 110587-110609. https://doi.org/10.1016/j.diamond.2023.110587

[17] Sivakumar A, Lidong D, Sahaya Jude D S, *et al.* Acoustic shock wave-induced chemical reactions: A case study of NaCl single crystal. J. Mol. Struct. 2024; 1312: 138490-138498. https://doi.org/10.1016/j.molstruc.2024.138490

[18] Irine Maria Bincy F, Oviya S, Kumar RS, *et al.* Acoustic shock wave-induced reversible phase transition (rhombohedral to hexagonal) of bismuth telluride. J. Mater. Sci., 2024; 59: 7044-7059. https://doi.org/10.1007/s10853-024-09574-9

[19] Oviya S, Irine Maria Bincy F, Arumugam S, *et al.* Acoustic shock wave-induced phase transition in indium selenide: Tuning band gap energy for solar cell applications. CrystEngComm, 2024; 26: 2498-2510. https://doi.org/10.1039/D4CE00012A

[20] Sivakumar A, Sahaya Jude D S, Pazhanivel T, *et al.* Phase transformation of amorphous to crystalline of multiwall carbon nanotubes by shock waves. Cryst. Growth Des., 2021; 21: 1617-1624. https://doi.org/10.1021/acs.cgd.0c01464

[21] Sivakumar A, Dai L, Sahaya Jude D S, *et al.* Acoustic shock wave-induced solid-state fusion of nanoparticles: A case study of the conversion of one-dimensional rod shape into three-dimensional honeycomb nanostructures of CdO for high-performance energy storage materials. Inorg. Chem., 2024; 63: 576-592. https://doi.org/10.1021/acs.inorgchem.3c03461

[22] Irine Maria Bincy F, Oviya S, Kumar RS, *et al.* Acoustic shock wave treatment as a pathway to enhance the specific capacitance of selenium-based layered chalcogenides for supercapacitor applications. New J. Chem., 2025; 49: 8297-8315. https://doi.org/10.1039/D5NJ00461F

[23] Irine Maria Bincy F, Oviya S, Kannappan P, *et al.* Acoustic shock wave-driven dynamic recrystallization induced reversible rod-to-cube morphology transition in CdS: preserving structural integrity with optical modifications. Dalton Trans., 2025; 54: 10916-10935. https://doi.org/10.1039/D5DT00998G

[24] Gao Y, Kong D, Han J, *et al.* Cadmium sulfide in-situ derived heterostructure hybrids with tunable component ratio for highly sensitive and selective detection of ppb-level H_2S. J. Colloid Interface Sci., 2022; 627: 332-342. https://doi.org/10.1016/j.jcis.2022.07.052

[25] Anirudha G, Sanhita P, Satyabrata R. Structural phase transformation from wurtzite to zinc-blende in uncapped CdS nanoparticles. Solid State Commun., 2013; 154: 25-29. https://doi.org/10.1016/j.ssc.2012.10.038

[26] Sivakumar A, Dai L, Sahaya Jude D S, *et al.* Tuning of lower to higher crystalline nature of b-L-glutamic acid by shock waves. J. Mol. Struct., 2023; 1288: 135788. https://doi.org/10.1016/j.molstruc.2023.135788

[27] Ichiyanagi K, Nakamura KG. Structural dynamics of materials under shock compression investigated with synchrotron radiation. Metals, 2016; 6: 17. https://doi.org/10.3390/met6010017

[28] Nasiri-Tabrizi B. Thermal treatment effect on structural features of mechano-synthesized fluorapatite-titania nanocomposite: A comparative study. J. Adv. Ceram., 2014; 3: 31-42. https://doi.org/10.1007/s40145-014-0090-4

[29] Pal M, Mathews NR, Santiago P, *et al.* A facile one-pot synthesis of highly luminescent CdS nanoparticles using thioglycerol as capping agent. J. Nanopart. Res., 2012; 14: 916. https://doi.org/10.1007/s11051-012-0916-3

[30] Khatter J, Chauhan RP. Gamma-ray induced modifications on CdS nanorod mesh: Structural, optical, and electrical properties. Radiat. Phys. Chem., 2021; 182: 109353. https://doi.org/10.1016/j.radphyschem.2021.109353

[31] Kong X, Yu F, Zhang H, *et al.* Synthesis and study of morphology regulation, formation mechanism, and photocatalytic performance of CdS. Appl. Surf. Sci., 2022; 576: 151817. https://doi.org/10.1016/j.apsusc.2021.151817

[32] Kanemitsu Y, Ishida Y, Nakada I, Kuroda H. Anomalous surface transformations in crystalline silicon induced by subpicosecond laser pulses. Appl. Phys. Lett., 1986; 48: 209-211. https://doi.org/10.1063/1.96797

[33] Riaz M, Ali B, Mansoor Ali S, *et al.* Stress-induced transformation on the cubic perovskite $RbTaO_3$ for high-temperature applications: a DFT approach. J. Comput. Electron., 2024; 23: 483-497. https://doi.org/10.1007/s10825-024-02166-5

[34] Sharma M, Murugavel S, Shukla DK, de Groot FMF. Reversal in lattice contraction of α-Fe_2O_3 nanoparticles. J. Phys. Chem. C, 2018; 122: 9292-9301. https://doi.org/10.1021/acs.jpcc.8b00550

[35] Liang YC, Lung TW. Growth of hydrothermally derived CdS-based nanostructures with various crystal features and photoactivated properties. Nanoscale Res., 2016; 11: 264. https://doi.org/10.1186/s11671-016-1490-x

[36] Meshcheryakov YI, Divakov AK, Atroshenko SA, Naumova NS. Effect of velocity nonuniformity on the dynamic recrystallization of metals in shock waves. Tech. Phys. Lett., 2010; 36: 1125-1128. https://doi.org/10.1134/S1063785010120187

[37] Sivakumar A, Dai L, Jude Dhas SS, *et al.* Experimental evidence of acoustic shock wave-induced dynamic recrystallization: A case study on ammonium sulfate. Cryst. Growth Des., 2024; 24: 491-498. https://doi.org/10.1021/acs.cgd.3c01180

[38] Shi J, Jiang B, Liu Z, *et al.* Effects of specific surface area of electrode and different electrolyte on capacitance properties in nanoporous-structure CrN thin film electrode for supercapacitor. Ceram. Int., 2021; 47: 18540-18549. https://doi.org/10.1016/j.ceramint.2021.03.177

[39] Ahmad G, Javed Y, Jamil Y, *et al.* Efficient label-free detection of chloramphenicol by iron-doped cadmium sulfide nanomaterials. J. Mater. Sci.: Mater. Electron., 2022; 33: 12295-12309. https://doi.org/10.1007/s10854-022-08188-8

[40] Zhang S, Huang W, Fu X, *et al.* Ultra-low content of Pt modified CdS nanorods: Preparation, characterization, and application for photocatalytic selective oxidation of aromatic alcohols and reduction of nitroarenes in one reaction system. J. Hazard. Mater., 2018; 360: 182-192. https://doi.org/10.1016/j.jhazmat.2018.07.108

[41] Nisha V, Paravannoor A, Panoth D, *et al.* CdS nanosheets as electrode materials for all pseudocapacitive asymmetric supercapacitors. Bull. Mater. Sci., 2021; 44: 101. https://doi.org/10.1007/s12034-021-02392-8

[42] Brijesh K, Nagaraja HS. Lower band gap $Sb/ZnWO_4$/r-GO nanocomposite-based supercapacitor electrodes. J. Electron. Mater., 2019; 48: 4188-4195. https://doi.org/10.1007/s11664-019-07185-8

[43] Augustyn V, Simon P, Dunn B. Pseudocapacitive oxide materials for high-rate electrochemical energy storage. Energy Environ. Sci., 2014; 7: 1597-1614. https://doi.org/10.1039/c3ee44164d

[44] Simon P, Gogotsi Y, Dunn B. Where do batteries end and supercapacitors begin? Science, 2014; 80: 1210-1211. https://doi.org/10.1126/science.1249625

[45] Muhammad A, Riaz J, Yang YH, *et al.* Synthesis of high-performance CdS/MnO composite electrode to achieve high energy and power densities for asymmetrical supercapacitors. Mater. Des., 2025; 251: 113704-113715. https://doi.org/10.1016/j.matdes.2025.113704

[46] Yan J, Fan Z, Wei T, *et al.* Fast and reversible surface redox reaction of graphene-MnO_2 composites as supercapacitor electrodes. Carbon, 2010; 48: 487-493. https://doi.org/10.1016/j.carbon.2009.09.066

[47] ul Haq Ali Shah A, Ullah S, Bilal S, *et al.* Reduced graphene oxide/poly(pyrrole-co-thiophene) hybrid composite materials: Synthesis, characterization, and supercapacitive properties. Polymers, 2020; 12: 1110-1131. https://doi.org/10.3390/polym12051110

[48] Deepannita C, Maruthamuthu S, Tholkappiyan R, *et al.* Zinc positioning's impact on electrochemical stability of γ-Al_2O_3 for supercapacitor efficiency. Ionics, 2024; 30: 7365-7380. https://doi.org/10.1007/s11581-024-05802-z

[49] Tholkappiyan R, Raji RK, Palanisamy S, *et al.* The role of in situ and operando techniques in unraveling local electrochemical supercapacitor phenomena. Ind. Eng. Chem. Res., 2025; 145: 144-168. https://doi.org/10.1016/j.jiec.2024.10.077

[50] Mahendiran R, Iyandurai N, Muniyappan M. Synthesis and characterization of strontium titanate ($SrTiO_3$) nanoparticles doped with Azadirachta indica leaf extract and coconut water by sol-gel method. Eur. Chem. Bull., 2023; 12: 184-198.

[51] Allison A, Andreas HA. Minimizing the Nyquist-plot semi-circle of pseudocapacitive manganese oxides through modification of the oxide-substrate interface resistance. J. Power Sources, 2019; 426: 93-96. https://doi.org/10.1016/j.jpowsour.2019.04.029

https://doi.org/10.66000/3110-9772.2025.01.02